2023

Granular materials. — In the first experiment shear induced orientational ordering of asymmetric elongated particles was investigated. Corn grains and pegs with one end sharpened were studied using x-ray computed tomography during quasistatic shearing and for flow in a 3-dimensional silo (see Fig. 1a). We have shown that asymmetries can be detected in the orientational distributions of the particles, which are related to the modulated rotation of the particles during shear flow [1]. In the second experiment (Fig. 1b) the flow of elliptical particles out of a 2-dimensional silo when extracted with a conveyor belt was analyzed. The conveyor belt—placed directly below the silo outlet—reduces the flow rate, increases the size of the stagnant zone, and it has a very strong influence on the relative velocity fluctuations as they strongly increase everywhere in the silo with decreasing belt speed. In other words, instead of slower but smooth flow, flow reduction by belt leads to intermittent flow. Interestingly, we show that this intermittency correlates with a strong reduction of the orientational order of the particles at the orifice region [2]. In the third experiment (Fig. 1c) we investigated the force of flowing granular material on an obstacle. In experiments with frictional hard glass beads, the force on the obstacle was practically flow-rate independent. In contrast, flow of nearly frictionless soft hydrogel spheres leads to a drag force which increases with flow rate. The dependence of the total force on the obstacle diameter is qualitatively different for the two types of material: it grows quadratically with the obstacle diameter in the soft, low-friction material, while it grows much weaker, nearly linearly with the obstacle diameter, in the bed of glass spheres [3].

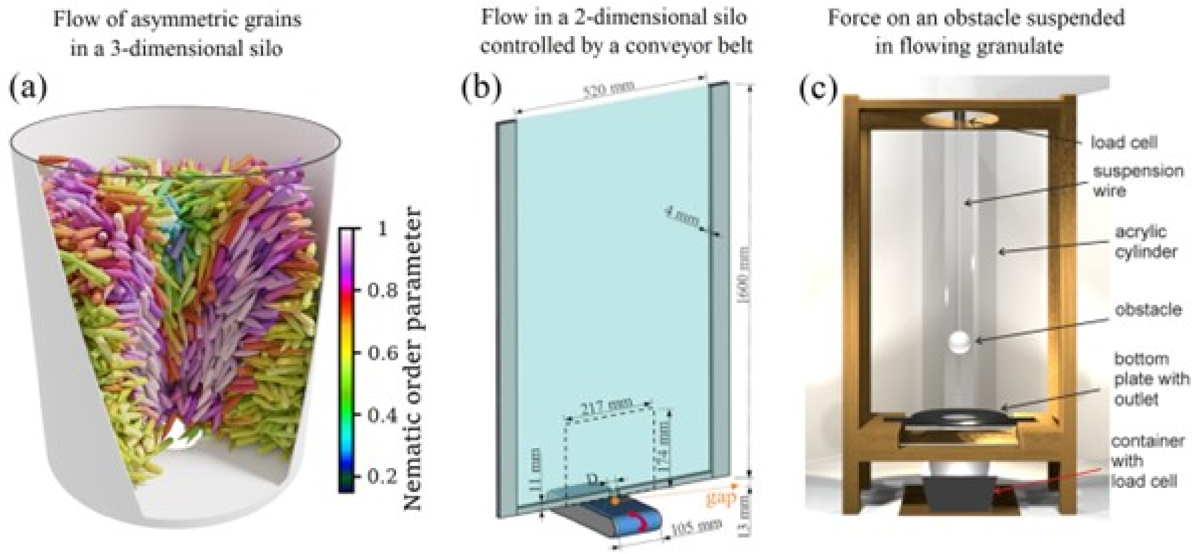
Flow of asymmetric grains in a 3-dimensional silo

Flow in a 2-dimensional silo controlled by a conveyor belt

Force on an obstacle suspended in flowing granulate

Figure 1. (a) Flow of asymmetric elongated grains in a 3-dimensional silo, (b) flow of elongated grains in a 2-dimensional silo when extracted with a conveyor belt, (c) force on an obstacle suspended in a flowing granular material.

Pattern formation in liquid crystals. – We studied droplets of a ferroelectric nematic fluid exposed to electric fields [4]. Above a threshold field, a new type of interfacial instability was found resulting in branched fractal-like structures as seen in Fig. 2. The phenomenon was explained by the interaction of the external electric field and the charges originating from the spontaneous polarization field, balanced by the surface tension of the fluid. The results are interpreted in analogy to the Rayleigh-type instability observed in charged droplets in electric fields and to surface instabilities observed in ferromagnetic liquids in magnetic fields. The nematic director and ferroelectric polarization direction was found to point along the tip of the fingers that appear to repel each other, resulting in strange interactions between neighboring droplets.

We discovered [5] layer undulations on micrometer scale in smectic-A liquid crystal phases appearing as regular stripe patterns induced by thermal treatment (Fig. 2c). Undulations, including their anharmonic properties, are evaluated by means of polarimetric imaging (Fig. 2d) and light diffraction experiments in cells with various thicknesses. The key role in stripe formation is played by high negative values of the thermal expansion coefficient.

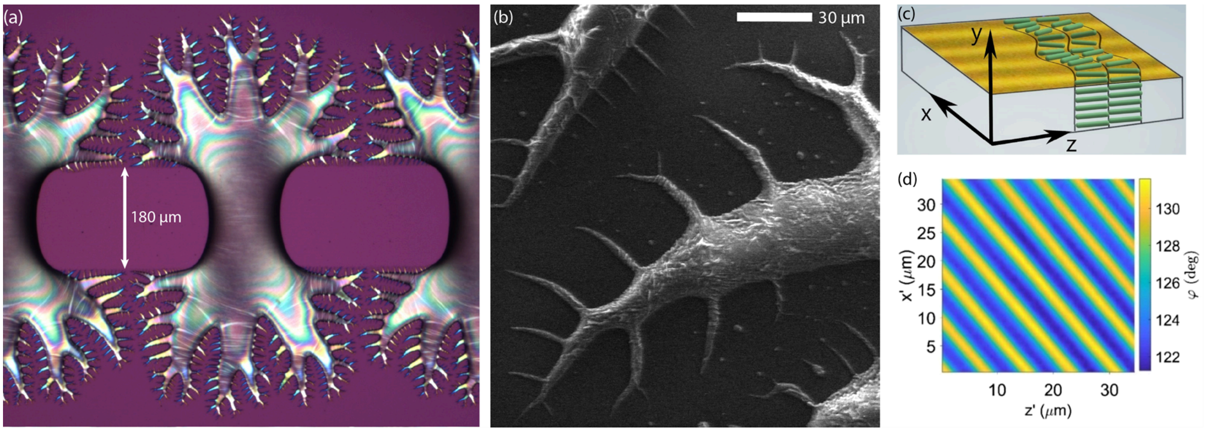

Figure 2. Fractal-like branched structures formed from spherical cap shaped ferroelectric nematic droplets exposed to electric fields, observed by (a) polarizing optical and (b) scanning electron microscopy. Thermal treatment induced stripe patterns of smectic-A layer undulations imaged by (c) polarizing and (d) polarimetric microscopy.

Polymer—liquid crystal interfaces. — We have compared photoaligning properties of polymer layers fabricated from the same constituents: polymethyl-methacrylate (PMMA) and azo-dye Disperse Red 1 (DR1), either chemically attached to the PMMA main-chain, or physically mixed with it [6]. Photoaligning properties depend on the preparation method drastically. Photoalignment was found to be far more efficient when PMMA is functionalized with DR1 compared to the case of physically mixing the constituents. This finding is supported by atomic force microscope (AFM) scans monitoring the light-induced changes at the polymer–air interface, and revealing a photo-induced mass transfer, especially in the case of functionalized PMMA (Fig. 3).

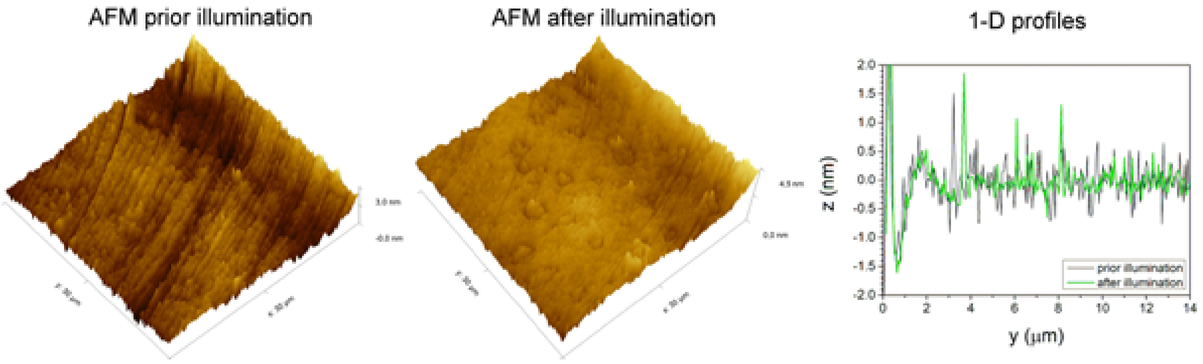

Figure 3. AFM scans on the functionalized PMMA surface and one-dimensional profiles along a line prior and after the illumination.

Electrodeposited nanostructures. — We prepared a near-equimolar Co–Fe–Ni–Zn multiple principal element alloy film by pulse plating [7]. The composition of the layer (Co32Fe27Ni21Zn20 with about ±1 % random fluctuation) was even both laterally and along the surface normal. The alloy film had a dominant face-centered cubic (fcc) structure with a body-centered cubic and an amorphous minor phases. The average grain size was as small as ~12 nm. The average hardness and elastic modulus determined by nanoindentation were 9.2 and 197 GPa, respectively. This hardness is much higher than the values reported formerly on fcc MPEAs processed by other methods (3.6–6.9 GPa) which can be explained by the very small grain size and the existence of the bcc and amorphous minority phases. The resulting hardness value is about 9 times higher than that of the hardest constituent element (i.e., Co), which indicated the applicability of nanocrystalline multiple principal element alloys as hard coating.

References:

[1] DOI: 10.1088/1742-5468/ad0831

[2] DOI: 10.1103/PhysRevE.108.044902

[3] DOI: 10.1103/PhysRevE.108.L062901

[4] DOI: https://doi.org/10.1038/s41598-023-34067-1
[5] DOI: https://doi.org/10.1103/PhysRevLett.131.228101

[6] DOI: 10.3390/polym15214271

[7] DOI: https://doi.org/10.1016/j.surfcoat.2023.129740

2022

Granular materials. — The time evolution of the discharge of a narrow silo was investigated for different granular materials made of spherical or elongated grains in laboratory experiments and with discrete element model (DEM) calculations [1]. For spherical grains, we confirmed the widely known typical behavior with constant discharge rate (see Fig. 1a). For elongated particles we find a peculiar flow rate increase for a certain range of the normalized orifice diameter D/d* before the end of the discharge process (see Fig. 1b). While the flow field is practically homogeneous for spherical grains, it has strong gradients for elongated particles with a fast-flowing region in the middle of the silo surrounded by a stagnant zone. The flow rate increase is connected with a suppression of the stagnant zone, resulting in an increase in both the packing fraction and flow velocity near the silo outlet.

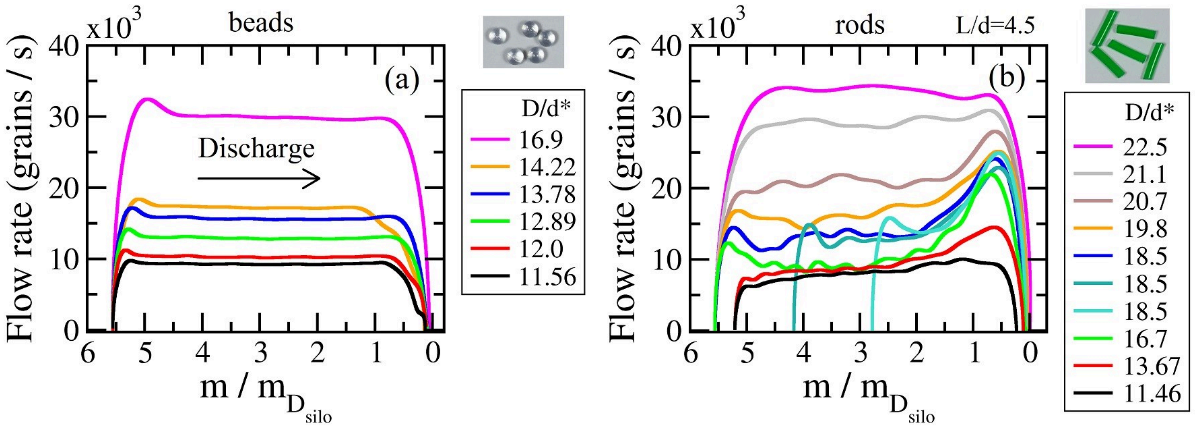

Figure 1. Silo flow rate as a function of the mass m in the silo for glass beads (left) and plastic rods with aspect ratio of L/d=4.5 (right). The value of m was normalized by the mass m_{Dsilo} of the material, corresponding to a filling height equal to the silo diameter.

Photo-sensitive mesogenic materials and surfaces. — A series of bent-core liquid crystals (LCs) possessing the azocinnamoyl unit in both elongating side arms was synthesized and characterized [2]. The chain length was kept fixed for each molecule ($C_{12}H_{25}$), whereas the substituents at the central and outer rings were varied. The LC phases were assigned by polarizing optical microscopy, differential scanning calorimetry and X-ray diffraction. The investigated compounds are suitably diverse to reveal some aspects of the relationship between molecular structure and the mesomorphic properties. Namely, non-substituted parent compound is crystalline only and the methyl group in position 2 or the chlorine atom in position 4 of the central ring suppresses LC phase formation. Introduction of the strong electron-withdrawing nitro group between the side arms on the central ring leads to a B7 phase (Fig. 2a). Compounds possessing a bromine atom or two chlorine atoms in the neighborhood of the ester groups form LC phases typical for rod-like molecules, namely a nematic – smectic phase sequence. The results are compared with those reported for the azobenzoyl analogues, and the UV illumination induced changes in the LC order have been revealed (Fig. 2b).

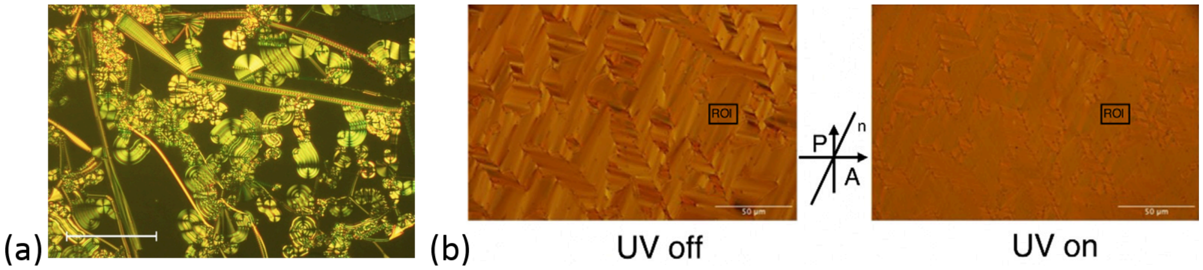

Figure 2. (a) Optical texture observed between crossed polarizers at the Iso-B7 phase transition. Scale bar represents 50 mm; (b) UV illumination-induced changes revealed by polarizing optical microscopy imaging.

We have summarized our results related to light-induced orientational phenomena at LC–polymer interfaces [3]. We investigated photoalignment for various nematics at the interface with the photosensitive polymer layer polymethyl methacrilate functionalized with azo dye Disperse Red 1, as well as with a polyimide layer in which Disperse Orange 3 was physically included. It was found that the efficiency of photoalignment exhibits marked differences depending on the structure of the rigid core of the liquid crystal molecules. It was demonstrated that the photo-orientation process is also significantly affected by the type of mesophase in which irradiation is carried out. The observations highlight the importance of the mutual influence of the polymer and the LC in light-induced processes.

Topology and patterns in liquid crystals tunable by electric and magnetic fields. – We revealed the structure of plano-convex lens-shaped nematic liquid crystal droplets (having potential for their use in tunable multifocal optical lenses) subjected to simultaneous competing magnetic and electric fields. A buckling instability of an initially straight defect wall was experimentally characterized and theoretically discussed (Fig. 3(ab), [4]). During our studies on the structure of ferroelectric nematic droplets (Fig. 3(cd)), we discovered and explained a new phenomenon in a ferroelectric nematic liquid crystal, namely an unexpected thermal gradient-induced circular flow observable only in the ferroelectric phase [5]. We characterized unusual electric-field-induced pattern forming scenarios in a new hockey-stick shaped liquid crystal (Fig. 3(ef), [6]).

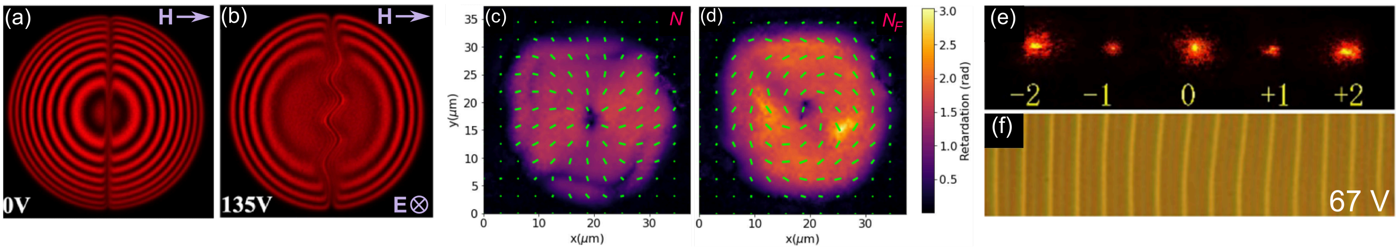

Figure 3. Polarizing microscopy images of nematic droplets exposed to (a) magnetic and (b) crossed magnetic and electric fields. (c-d) Structure of a polar liquid crystal droplet in the normal (N) and ferroelectric nematic (N_F) phase revealed by polarimetric microscopy. (e-f) Electric-field-induced pattern in a hockey-stick shaped liquid crystal and light diffraction on them.

Electrodeposited nanostructures. — The crystal structure of electrodeposited cobalt foils prepared under different conditions was studied with several methods (X-ray diffractometry in both Bragg–Brentano and transmission geometry, transmission electron microscopy) [7]. Stable hexagonal close-packed (hcp) Co could be electrodeposited at relatively small current density from a solution with a pH of about 5. On the other hand, from low-pH solutions and with high current densities, we could obtain Co deposits with as high as 75 % fraction of the metastable face-centered cubic (fcc) phase. With intermediate deposition conditions, a phase mixture is obtained. The surface morphology of the samples of various types is very characteristic, as shown in Figure 4.

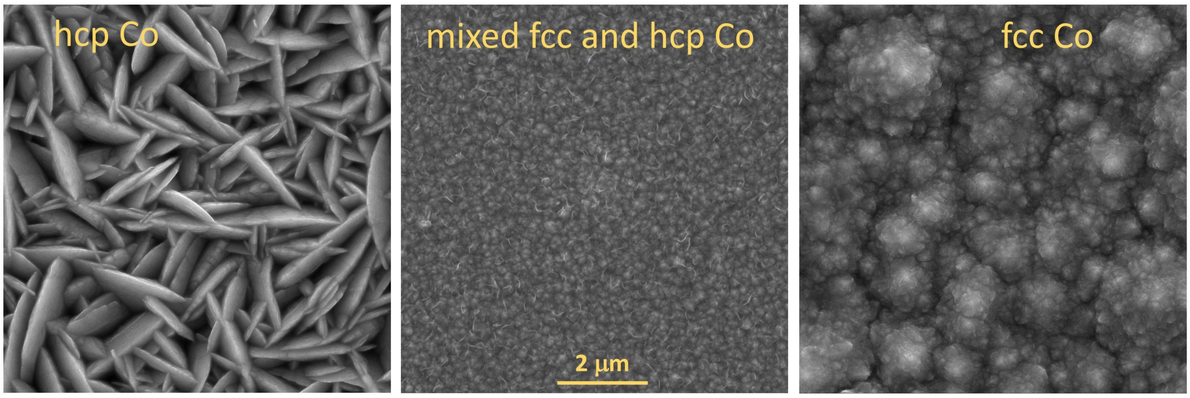

Figure 4. Scanning electron micrographs of Co samples of various phase composition.

In spite of the large number of earlier reports on the magnetoresistance of cobalt metal published in the last 140 years, only our present study was suitable to rate the anisotropic magnetoresistance (AMR) of these two crystalline modifications of cobalt. The AMR ratio of hcp-Co was found to be 1.20 %, while the AMR ratio of fcc-Co was estimated to be about 2.16%.

2021

Granular materials. — Silo discharge was studied with traditional (frictional hard) granular materials as well as with soft low friction grains [1]. Particle stiffness has a strong effect on the flow rate. For deformable grains lowering the friction coefficient leads to a gradual change in the discharge curve: the pressure near the orifice as well as the flow rate becomes filling height dependent, they decrease during the discharge process (see Fig. 1a). For hard grains the flow rate is much less sensitive to the value of the friction coefficient, the pressure is not height dependent, and silo discharge happens with constant flow rate (see Fig. 1b). Silo flow was also studied with mixtures of frictional hard and soft low friction grains [2]. In a 2D silo the addition of a small amount (5-10%) of hard grains significantly changes the flow behavior. Experiments with a silo with a rotating bottom have also been performed with elongated grains [3]. In another study we analyzed the statistical properties of granular packings in a nearly two-dimensional box (see Fig. 1c) to test Edwards approach based on equiprobable jammed states. When tapped, the system evolves toward a ground state, but due to incompatible domain structures it gets trapped [4].

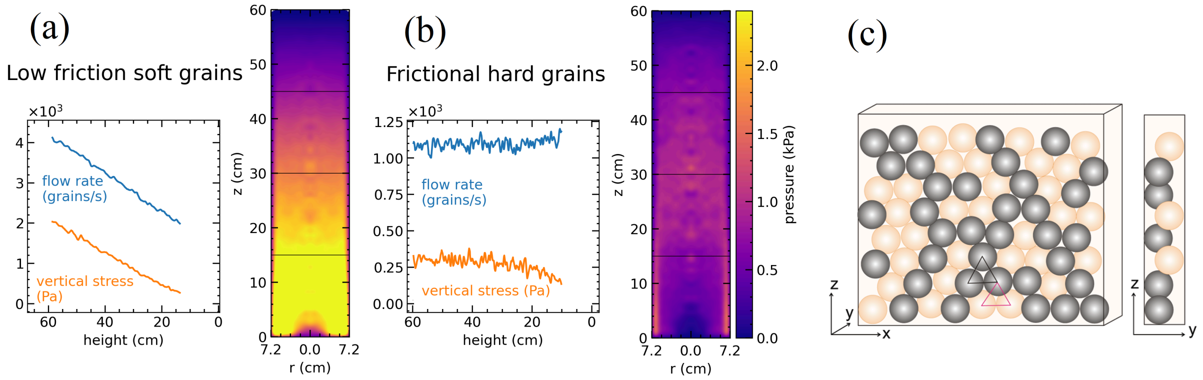

Figure 1. Silo discharge with (a) soft low friction grains and with (b) traditional (frictional hard) granular material. (c) Disordered packing of spheres confined in a nearly two-dimensional box.

Photo-sensitive mesogenic materials and surfaces. — A series of asymmetric bent-core liquid crystals, bearing the stilbene moiety in the side wing, was synthesized and characterized [5]. A new liquid crystal dimer, exhibiting enantiotropic nematic phase, was synthesized and structurally characterized. The spectroscopic properties were analyzed by UV–Vis and fluorescence techniques. Theoretical calculations were used to predict the UV–Vis spectral properties of three isomers (Fig. 2a) and propose a mechanism of conversion between them [6]. Experimental evidence was provided for the influence of the molecular structure of the nematic liquid crystal (NLC) on the photoalignment process in three dimensions at the interface with a polymer layer. Findings were explained through the presence (or absence) of a π - π aromatic interactions between the NLC and the polymer. The influence of the nematic-to-smectic A phase transition on the photocontrol was also addressed [7].

Liquid crystal composite materials. — Experimentally was demonstrated that the anchoring of a nematic liquid crystal on a solid substrate together with the anchoring of the liquid crystal on a nanoparticle surface induces orientational self-assembly of anisometric nanoparticles in sessile liquid crystal droplets (see Fig. 2b). The observed phenomenon opens a novel route for fabrication of thin colloidal films with tailored properties [8].

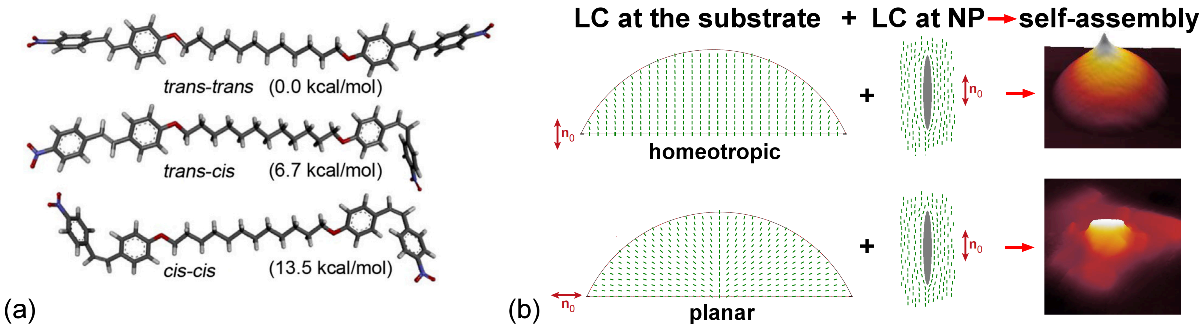

Figure 2. (a) The optimized structures of three isomer forms of the new liquid crystal (LC) dimer. (b) Anchoring of LC at the substrate and at the nanoparticle (NP) defines the orientational self-assembly of anisometric NPs in sessile LC droplets.

Topology of liquid crystals in lens shaped confinement. – We discovered temperature induced molecular orientational (anchoring) transitions in nematic fluids at solid and at air interfaces. We established a rapid method based on sessile droplets to find anchoring transitions. Different types of defect structures were understood by optical simulations depending on the different boundary conditions. Discontinuous, continuous, and re-entrant (Fig. 3(a)) anchoring transitions were identified [9]. Optical textures of lens shaped liquid crystal droplets have been studied in electric fields (Fig. 3(b)). We observed the formation of inversion walls normal to AC electric fields and their motions. The movement of the defect walls at low and high frequencies was explained [10].

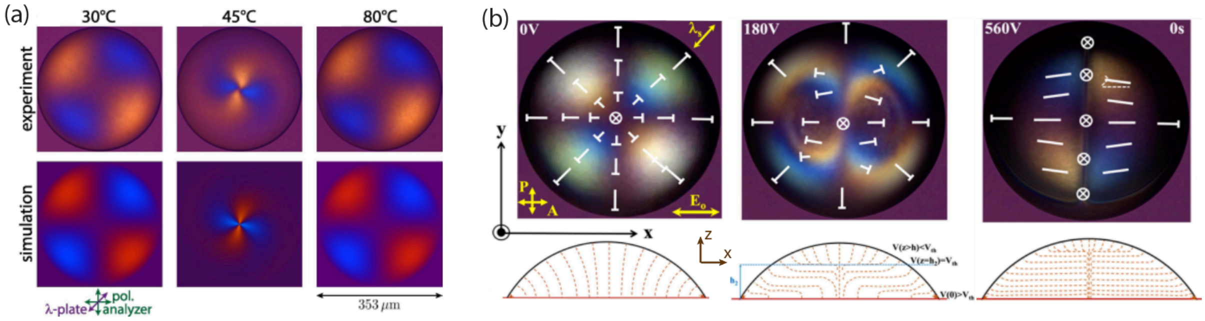

Figure 3. (a) Experimental and simulated textures of a sessile droplet of the liquid crystal I52 at different temperatures in the nematic phase (b) Polarizing micrographs of a sessile droplet of the liquid crystal 5CB under different levels of in-plane electric fields.

Light tunable gratings in liquid crystals. — Electroconvection patterns with UV light tunable wave vector were found in a hybrid aligned cholesteric liquid crystal containing a chiral photosensitive dopant [11]. The UV irradiation rotates the pattern via alteration of the helical pitch. The magnitude and direction of the rotation angle depends on the UV light intensity (Fig. 4), the concentration and type of the chiral dopant. Applicability of the effect for two-dimensional beam steering was demonstrated.

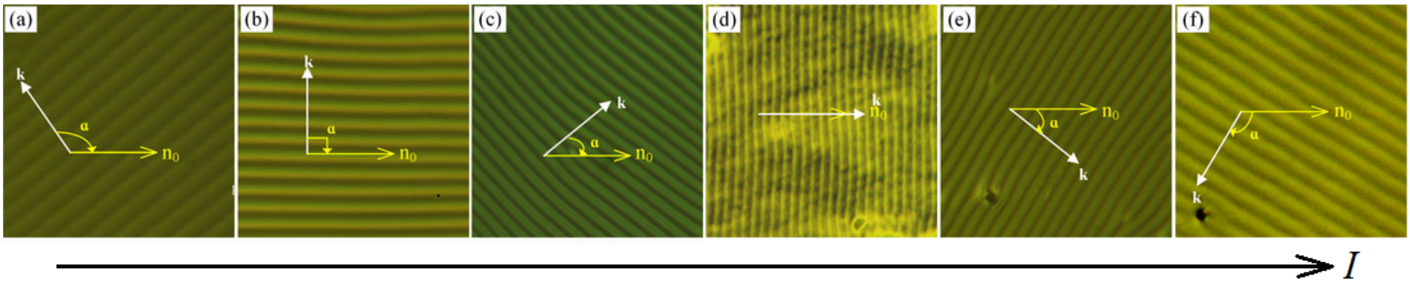

Figure 4. Snapshots of rotatable electroconvection rolls in the initially right-handed cholesteric taken after 60 seconds of UV illumination with increasing intensities. (a)–(c) right-handed helix; (d) compensated cholesteric (unwound) state; (e)–(f) left-handed helix.

Electrodeposited nanostructures. — Structure of electrodeposited Ni–Mo alloys up to 6 at.% Mo content were analyzed in detail [12]. Beside the often reported properties (such as Mo content and grain size), special properties obtained from the convolutional multiple whole profile fitting of the X-ray diffractograms were also analyzed (such as dislocation density and twin formation probability). It was established that clear trends can be established for the above-mentioned sample properties as long as a homogeneous sample series is investigated and the samples differ in one single preparation parameter only (see Figure 5). However, nominally “identical” samples (same Mo content and grain size) differ significantly in the other parameters if they are not the members of a homogeneous sample series.

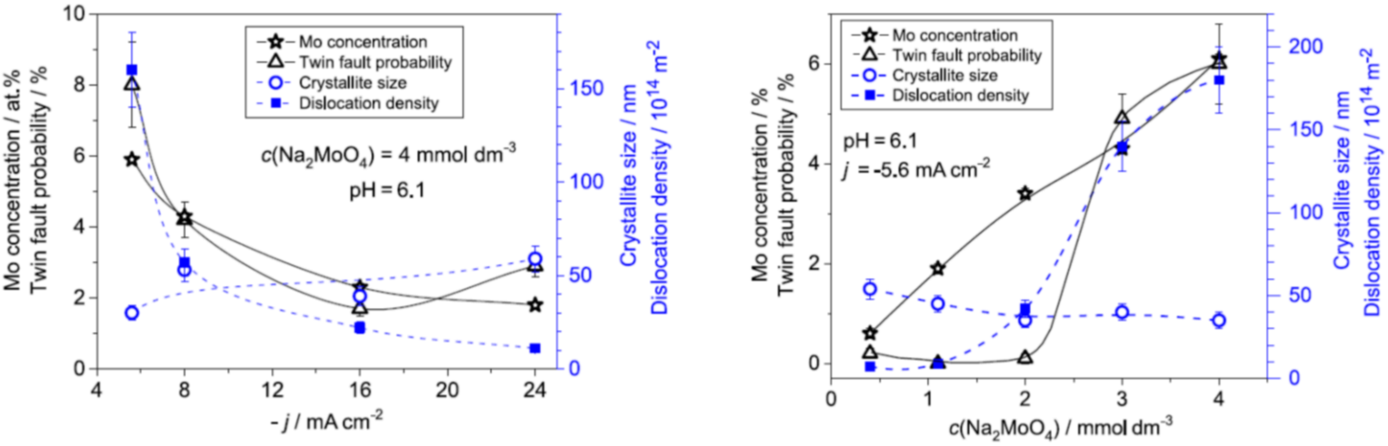

Figure 5. Variation of the structural properties of Ni–Mo alloys in two sample series. Left: impact of the current density; right: impact of the concentration of the precursor material.

A comprehensive analysis of the grain-boundary resistivity of Ni and Cu was given [13]. It was shown that grain size as obtained from X-ray diffractograms is misleading for the calculation of the grain-boundary resistivity since low-angle grain boundaries typically do not cause electron scattering. Therefore, grain sizes determined with direct imaging methods (such as transmission electron microscopy) are only relevant from the viewpoint of electron transport. Models developed for grain boundary resistivity were critically analyzed and the grain-boundary resistivity for Ni and Cu was determined from an extensive historical data base.

2020

Granular materials. — The rheology of frictional spherocylinders was investigated in shear flows [1]. We explored how the effective friction μ_c of the system changes with the inertial number, the interparticle friction coefficient μ_p and the particle aspect ratio L/D. For frictional grains the effective friction increases with the elongation of the particles, while for low friction particles a non-monotonic behavior is observed (see Fig.1). Silo discharge was studied numerically for the case of a silo with a rotating bottom plate. We show, that in accordance with recent experimental findings, for intermediate orifice diameter the discharge rate shows a non-monotonic behaviour on the rotation frequency of the bottom plate [2].

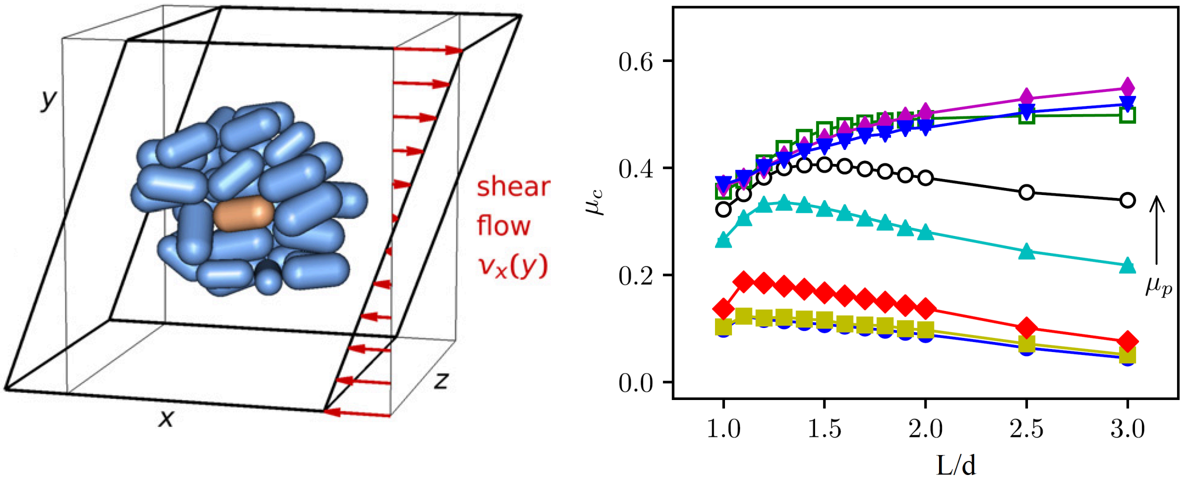

Figure 1. *The rheology of a sheared granular system consisting of frictional spherocylinders was investigated numerically.*

Suspension rheology. - We investigated rheological, viscoelastic and rheo-optical properties of a dispersion of anisometric pigment particles at various volume fractions. We demonstrated that increasing volume fraction leads to a transition from a non-Newtonian flow behaviour to a viscoelastic response with a high storage modulus. A giant effective stress-optical coefficient was found (higher than in other reported cases) which is connected to the flow alignment of the elongated nanoparticles [3].

Tunable liquid crystal lenses. - We studied the behavior of liquid crystal lens-shape drops in magnetic fields and found that the spatial variation of the director becomes very complex, involving a defect wall that moves in time. We proposed a theory to explain the experimental observations and showed how to suppress the defects [4].

Photo-sensitive mesogenic materials and surfaces. — The influence of the molecular structure of the nematic liquid crystal (NLC) on the photoalignment process at the NLC–polymer interface has been investigated experimentally. NLCs having exclusively phenyl-, or cyclohexane rings in the rigid core, as well as NLCs containing both phenyl and cyclohexane groups have been considered. Substantial differences have been found in the photoalignment process depending on the molecular structure of the NLC, for which a phenomenological explanation has been given [5].

Liquid crystal composite materials. — The dynamic magnetic susceptibility of ferronematics has been measured for high concentrations of nanoparticles. For a given composition of the ferronematic we have found the optimal concentration of the magnetic particles, for which the largest relative enhancement of the dynamic magnetic susceptibility is obtained upon the application of a bias magnetic field in the isotropic phase [6].

Electrodeposited nanostructures. — Various electrodeposited Ni-based coatings were studied with highly efficient structure analysis methods. Nickel electrodeposition was optimized by using cysteine as bath additive. The grain size of the Ni deposit was in the range of 20-30 nm in the 0.2-0.4 g/liter cysteine concentration, which was accompanied by a saturation of the Vickers hardness of the deposit in the same additive concentration range. In contrast to the grain size, both the twin fault probability and the dislocation density increased monotonically with the cysteine concentration. Although the annealing of the deposit up to 1000 K led to grain coarsening coupled with the annihilation of both the twins and the dislocations, a hardness optimum was found at an intermediate annealing temperature where the Vickers hardness value of 8400 is the largest reported for Ni in the literature. For electrodeposited Ni-Mo alloys, the compression behavior was studied in relation to the structural parameters. As a function of the Mo concentration, both strain hardening and strain softening could be observed. Softening was explained with de-twinning during the deformation. The room-temperature magnetoresistance characteristics of electrodeposited nanocrystalline Ni samples with various grain sizes were investigated. The anisotropic magnetoresistance ratio (AMR) for polycrystalline Ni metal amounts to 2.4 % and seems to be fairly independent of the microstructural features and grain sizes, which means that the AMR ratio is an inherent characteristics of the Ni metal matrix.

A review paper was published on the historical evolution and the recent elucidation of the term of electrochemical polarization. We analyzed the impact of the improvement in experimental methodology on the use of the “polarization” in the electrochemical literature and confronted its common meanings with various textbook definitions. Suggestions were made to resolve the contradictions between the traditional definitions and the modern practice [7].

2019

Photorheological liquid crystal dimer. — We showed that a liquid crystal dimer can behave as a photorheological material that can turn from a solid state (Fig. 1, brown) to a low viscosity fluid (Fig. 1, blue) by UV light illumination (Fig. 1, purple) [1,2]. This phenomenon can be explained by considering that the dimer molecules undergo a significant shape change as an effect of UV light. The fast photorheological phenomenon can provide the basis of a number of applications, for example in light switchable glues, vibration dampening or brakes. Our results were highlighted in the inside front cover of the journal Advanced Materials Interfaces.

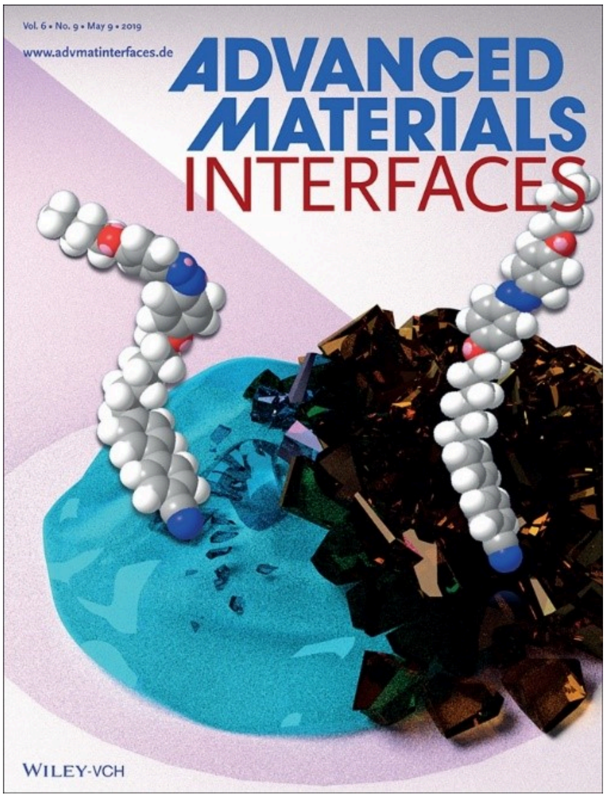

Figure 1. At a constant temperature, the solid material turns to be liquid by the effect of UV light.

Light tunable flexoelectric gratings. — We have studied a new photoresponsive bent-core nematic (BCN) material, which exhibits flexoelectric domains (FDs) driven by electric field. It was found that the wavelength of FDs can be controlled by irradiation with light fields [3]. This light tunability was ascribed to the photoisomerization effect of the azo moiety within the BCN molecules. The ratio of *trans* and *cis* isomers changes according to the colour and intensity of the illuminating light field: UV light increases the electric threshold and the periodicity of FDs, while blue light has an opposite effect. The phenomenon allows creation of optically controllable gratings, to be used in tunable photonic devices.

Flow properties of a granular material consisting of deformable particles with low surface friction. — We have studied the discharge of a silo with ultrafast X-ray tomography as well as regular X-ray tomography comparing the flow properties of usual granular materials (hard, frictional grains) and a material consisting of deformable particles with low surface friction. For hard frictional grains (Fig. 2), flow is concentrated in the middle part of the bin (red region) with stagnant zones near the wall, for low friction soft grains we find grain motion everywhere in the bin (Fig. 2, right image) [4,5].

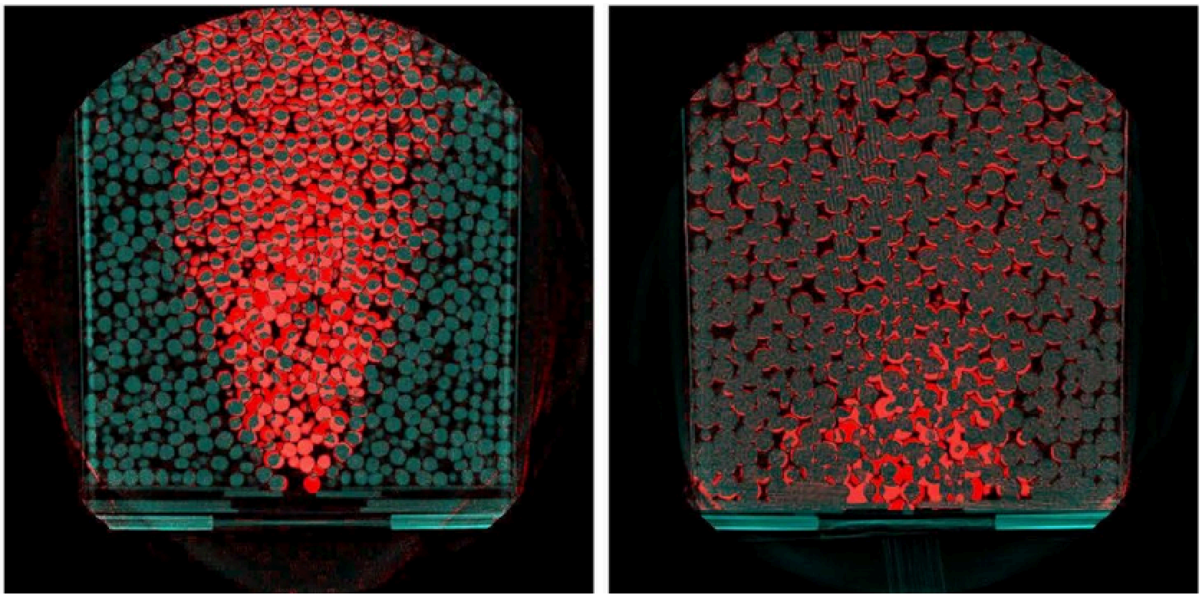

Figure 2.

Photo-sensitive mesogenic materials and surfaces. — Experimental evidence has been provided that photoalignment at the nematic liquid crystal (NLC)-polymer interface cannot be simply considered as a two-dimensional process (Fig. 2). Moreover, the experiments clearly indicate that the photoaligning process does not depend on the individual properties of the NLC material and those of the interfacing polymer exclusively. The polymer and the NLC layer interact, i.e., the polymer-liquid crystal interface should be regarded as a coupled system, where the two components mutually influence each other – see Fig. 2(a). Furthermore, it has been shown that the temperature induced anchoring transition also has to be taken into account for the complete description of the photoalignment mechanism [6] – see Fig. 2(b).

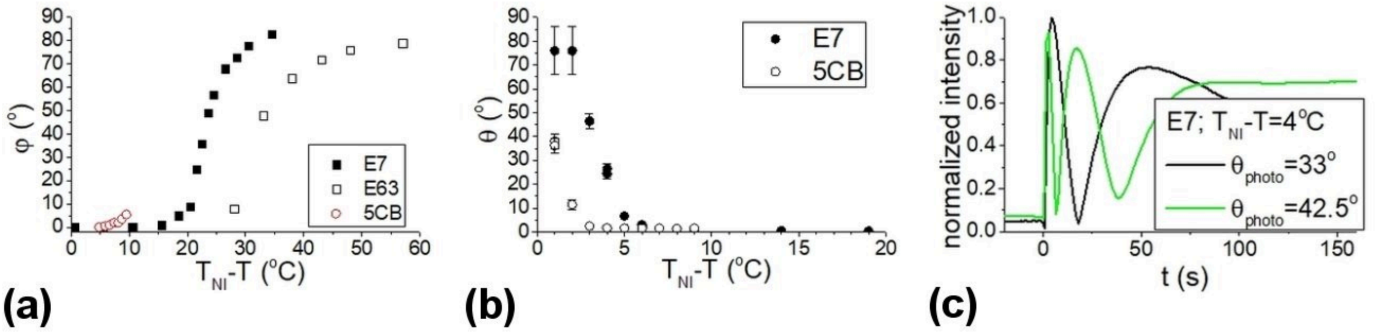

Figure 3. (a) Temperature dependence of the azimuthal photoalignment angle, φ for three NLCs; (b) Temperature induced change of the pretilt angle, θ; (c) Temporal evolution of the transmitted light intensity, demonstrating considerable values of the zenithal photoalignment angle, θ_{photo}.

The specific grain-boundary electrical resistivity of Ni. — The purpose of the present study [7] was to provide a reliable value for the specific grain-boundary resistivity ρ_{SGBR} of Ni metal. New results were presented on the room-temperature electrical resistivity of nanocrystalline (nc) Ni metal samples produced by electrodeposition with various grain sizes: The structural studies were carried out in collaboration with the Research Institute for Technical Physics and Materials Science of the Energy Research Centre and the Materials Physics Department of the Eötvös University, Budapest. The obtained resistivity data were analyzed by using the theory that the resistivity increment due to grain boundaries is proportional to the grain-boundary surface area per unit volume, which is equivalent the inverse proportionality of the grain boundary resistivity with the grain size. It was pointed out that the grain size determined by transmission electron microscopy imaging is the relevant parameter for the evaluation of ρ_{SGBR}. From the evaluation of the nc-Ni resistivity data at room temperature, it was found that $4.45\cdot10^{-16}\ \Omega\cdot m^2 < \rho_{SGBR}(Ni) < 6.2\cdot10^{-16}\ \Omega\cdot m^2$, and our upper bound of this interval agrees exactly with the most recent calculated value in the literature.

Structure and giant magnetoresistance of Co-Fe/Cu multilayer films electrodeposited from various bath formulations. — Detailed new results were reported [8] on the preparation and giant magnetoresistance (GMR) of electrodeposited Co-Fe/Cu multilayer films by using four different baths (sulfamate, sulfate, ammonium chloride and sodium citrate type solutions). Two-pulse plating was applied for Co Fe(5nm)/Cu(5nm) multilayer preparation by using galvanostatic pulses for the deposition of the magnetic layer. The Cu layer deposition potential was electrochemically optimized for each bath formulation by analyzing the current transients during the deposition of the non-magnetic layers. The optimal Cu deposition potential was found to be dependent both on the bath formulation and the Fe^{2+}/Co^{2+} ion concentration ratio. The results of X-ray diffraction (XRD) measurements carried out in collaboration with the Materials Physics Department of the Eötvös University, Budapest, were in agreement with the composition of the samples. At low Fe content (about 10 at.% Fe) in the magnetic layer, an fcc structure was formed and, in some cases, even multilayer satellites were observed as demonstrated in the left panel of Fig. 4). In samples with high Fe content (about 33 at.% Fe) in the magnetic layer, both fcc and bcc phases were present (right panel of Fig. 4). A GMR behavior was observed for all multilayers, with a maximum GMR of about 4 % in some cases. For multilayers from the sulfamate, sulfate and chloride baths, the GMR exhibited a multilayer-type behavior whereas the GMR of samples from the citrate bath was rather similar to the behavior of granular magnetic alloys containing also superparamagnetic regions.

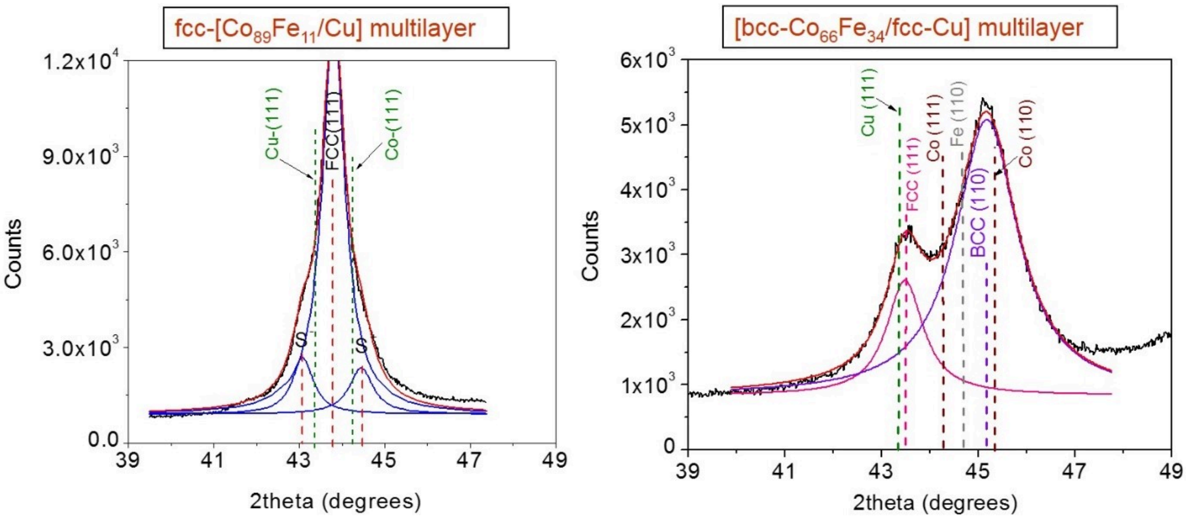

Figure 4. XRD patterns for Co-Fe(5nm)/Cu(5nm) multilayers prepared from a sulfamate bath (pH = 3.6) with j_{magn} = 20.7 mA/cm^2 from baths with $c_{ion,Fe}$ = 5 mol% (sample 1, left panel) and with $c_{ion,Fe}$ = 20 mol% (sample 3, right panel). The vertical dashed lines indicate the peak position of the relevant reflections.

External links:
[1] https://doi.org/10.1002/admi.201802032
[2] http://dx.doi.org/10.3791/60433
[3] https://doi.org/10.1002/adom.201801790
[4] https://doi.org/10.1088/1367-2630/ab5893
[5] https://doi.org/10.1007/s10035-019-0910-x
[6] https://doi.org/10.1016/j.molliq.2019.04.074
[7] https://doi.org/10.1080/14786435.2019.1580399
[8] https://doi.org/10.1149/2.0391916jes

2018

Granular materials. — Flow, rheology and packing of granular materials.

The stationary flow field in a quasi-two-dimensional hopper (Fig. 1a) was investigated experimentally. The behavior of materials consisting of beads and elongated particles with various aspect ratios was compared. We show, that while the vertical velocity in the flowing region can be fitted with a Gaussian function for beads, in the case of elongated grains the flowing channel is narrower and is bordered with a sharper velocity gradient (Fig. 1b). For this case, we quantify deviations from the Gaussian velocity profile. Relative velocity fluctuations are considerably larger and slower for elongated grains (Fig. 1c).

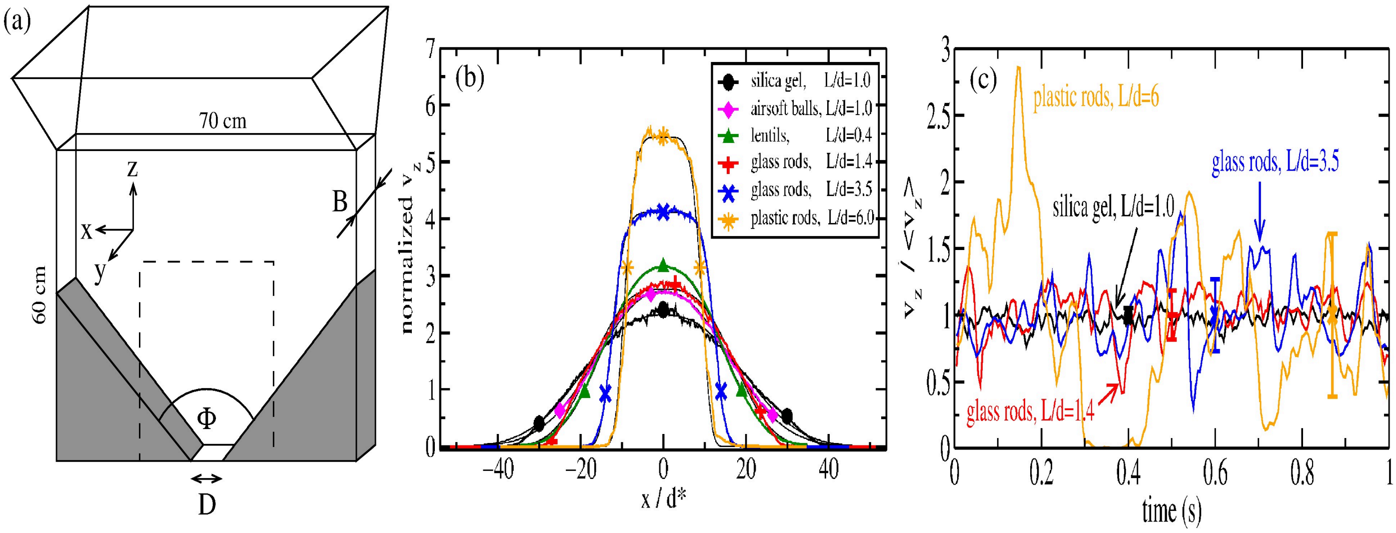

Figure 1. *(a) Sketch of the quasi-two-dimensional hopper, (b) vertical velocity across the hopper, (c) time evolution of the vertical velocity.*

The rheology of non-spherical granular particles has been investigated in inclined plane flows. Our discrete element simulations and laboratory experiments revealed that density and friction are well-defined functions of the effective inertial number, which fully captures the effect of grain elongation.

We studied the packing of spheres experimentally and numerically in 2 + ε dimensions, realized by a container which is in one dimension slightly wider than the spheres. The particles organize themselves in a triangular lattice, while touching either the front or rear side of the container. This system appears to be similar to a frustrated spin-glass, but it has a well defined ground state built up from isosceles triangles. When the system is agitated, it evolves very slowly towards the potential energy minimum through metastable states. We show that the dynamics is local and is driven by the optimization of the volumes of 7-particle configurations and by the vertical interaction between touching spheres.

Liquid crystals – We studied a stable lattice of topological defects appearing at the electric reorientation of a nematic fluid by quantitative polarimetry and by laser diffraction. The generation of optical vortices by topological defects was achieved and demonstrated in cases of two distinct mechanisms. First, individual defects convert circularly polarized light partially into a vortex beam with opposite handedness (Fig. 2a and 2b), while beams diffracted on the defect lattice do not carry vorticity. Second, dislocation of the lattice structure is a topological defect on a larger length scale; then beams diffracted on a single dislocation possess optical vortex character. For both cases, the vortex-generation efficiency is tunable by the applied voltage.

We studied the bending of liquid crystal membranes with phospholipids. The interactions of phospholipids with liquid crystals have formed the basis for attractive biosensor technologies. Phospholipids turn the liquid crystal director perpendicular to the LC/water interface. If the other side of the LC film is in contact with a surface that prefers perpendicular alignment, the LC film appears completely dark between crossed polarizers. Increasing the lipid concentration, the liquid crystal texture brightens again. We showed by optical surface profiler measurements (see Fig. 2) that the interface of the LC film suspended in a transmission electron microscopy (TEM) grid bends towards the lipid-coated interface. We demonstrated that where the bending occurs, the bent interface exhibits extreme sensitivity to air pressure variations, producing an optical response with acoustic stimulation. We suggested a physical mechanism for this result.

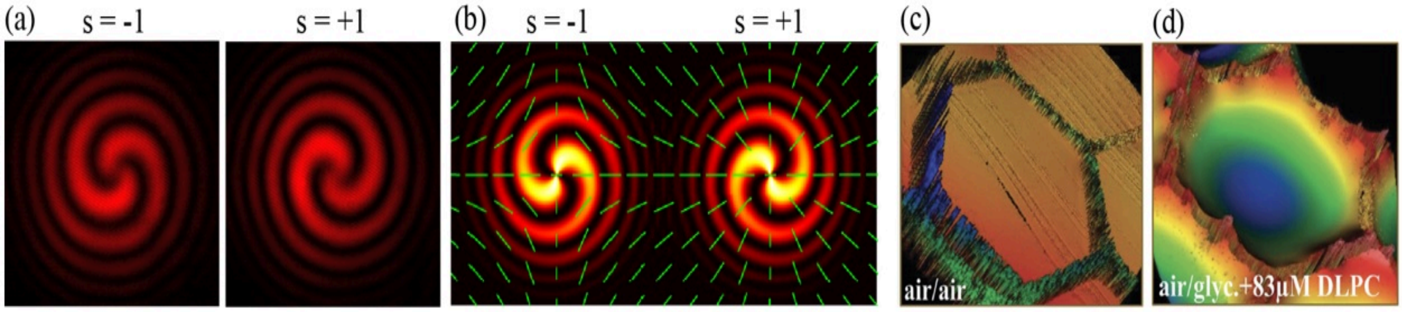

Figure 2. *Liquid crystal defect (with topological charge s =±1) generated optical vortices confirmed by interferometry: (a) experiments, (b) simulation. Liquid crystal membrane profiles with air on both sides (c) and with glycerol+pohospholipid on one side (d).*

The influence of UV light-induced pitch contraction and dilation on the electroconvection patterns (ECPs) of a chiral nematic liquid crystal containing a photoresponsive chiral dopant was investigated in planar-aligned cells. The helical twisting power of the dopant changed (even underwent handedness inversion) under UV irradiation; consequently, the pitch and the direction of the convection rolls in ECPs (being either parallel with or perpendicular to the surface alignment) could be controlled by the UV intensity and the ac voltage. The method of applying a light field allows a remote, contactless manipulation of the pitch, detectable via the morphological changes of ECPs, which can be utilized as a switchable optical grating.

In collaboration with German theoreticians a concise theoretical description has been developed for the nonlinear regime of the dc electric field induced flexodomains of planar nematic liquid crystals. Experiments on different nematics demonstrated that the wave number increases almost linearly with the applied voltage. This behavior was confirmed by approximate analytical as well as precise numerical calculations.

Liquid crystal composite materials. — Magnetic field induced shift of the isotropic-to-nematic phase transition temperature has been measured in neat bent-core and calamitic liquid crystals (LCs), in their mixture, and in samples doped with spherical magnetic nanoparticles (i.e., in so called ferronematics – FNs) for two different orientations of the magnetic field. A magnetic-field-induced negative or positive shift of the transition temperature was detected depending on the magnetic field orientation with respect to the initial orientation of the nematic phase, and on the type of liquid crystal matrix as illustrated in Fig.3.

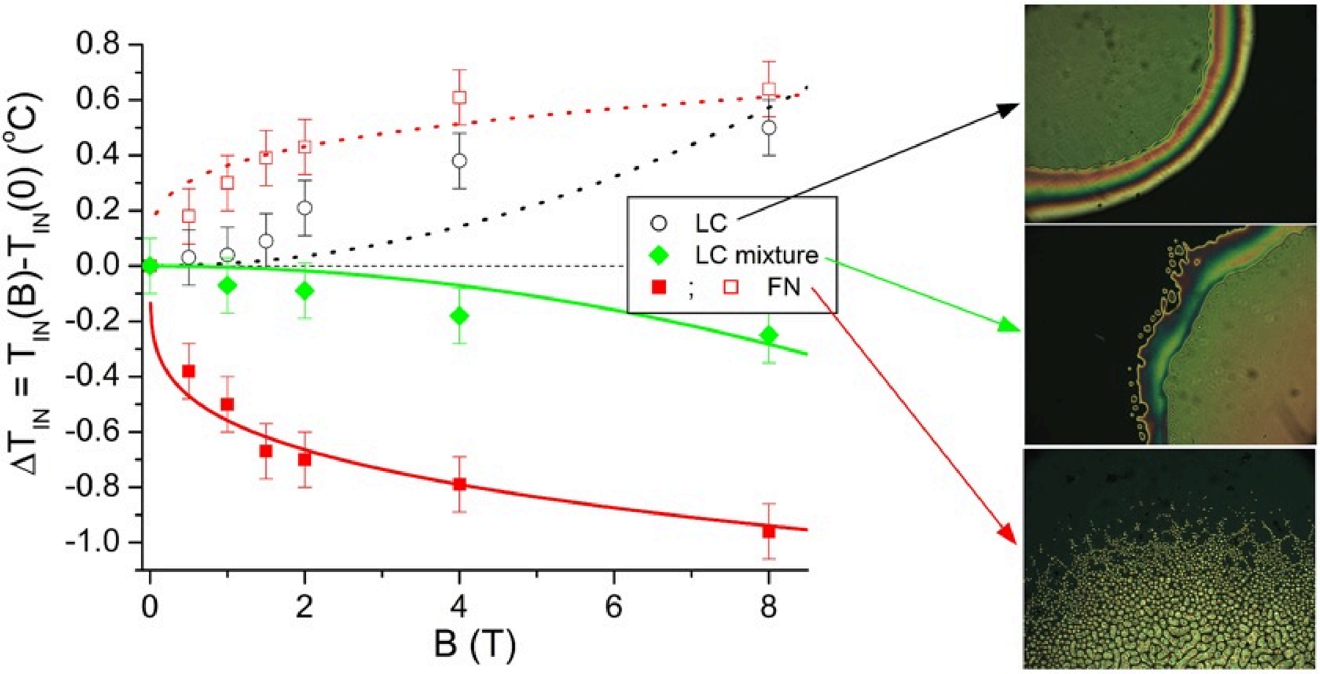

__Figure 3.__ Magnetic field-induced phase transition temperature shifts detected in a calamitic liquid crystal (LC), in its mixture with a bent-core LC, and in a ferronematic (FN) based on them. The lines represent theoretical fits. On the right: microphotographs of the isotropic-to-nematic phase transition in these systems.

Photo-sensitive mesogenic materials and surfaces. — In planar nematic liquid crystals cells twist deformation was generated through photoalignment. By increasing the twist angle gradually, supertwisted cells were constructed in the range of 2π–3π twist angle. The supertwist relaxed through the formation of either π or 2π inversion loops, depending on the character of the photosensitive substrate. The difference in the relaxation process was related to the zenithal anchoring strength on the photosensitive plate.

Magneto-sensitive surfaces. — We investigated the surface topographical modifications of a soft magnetoactive elastomer in response to magnetic fields. Optical profilometry analysis showed that the magnetic field-induced surface roughness with respect to magnetic field is in the range of 1 mm/T. Sessile water droplet shape analysis revealed that the field-induced topographical modifications affect the contact angle at the surface. This effect is reversible and the responsivity to magnetic field was found in the range of 20°/T. Despite the increased surface roughness, the apparent contact angle decreases with increasing field, which is attributed to the field-induced protrusion of hydrophilic microparticles from the surface layer.

Component distribution of electrodeposited alloys. — Electrodeposited alloys prepared with constant current density exhibit a unique near-substrate component distribution. The preferentially deposited metals accumulate near the substrate, and the decay of the initial zone of uneven composition is 150-200 nm thick regardless of the alloy constituents. This effect has a great important in the deposition of nanostructures in which the total layer thickness is often less than the decay length scale of the spontaneous composition variation. It was shown that two countermeasures can provide deposits with even composition also in the near-substrate zone: a, application of pulse plating, and b, the application of uniform convection conditions. The results related to many deposit compositions were summarized in a comprehensive review article.

Special attention was devoted to the composition depth profile of Fe-Co-Ni deposits. It was shown that the composition variation as measured with either sputtering-based depth profiling methods or cross-sectional scans in a transmission electron microscope (TEM) are essentially identical. The advantage of the application of the TEM was that the length scale of the composition variation and that of the change in the crystallographic properties (grain size and orientation) could be seen for identical samples. It was revealed that variations in the composition and in the crystallographic properties are independent of each other. (This work was performed in co-operation with the Josef Stefan Institute, Ljubljana, Slovenia.)

Structural properties of electrodeposited metals. — The structural properties of electrodeposited nanocrystalline Ni films were analyzed with TEM and X-ray line profile analysis (XLPA). The effect of saccharin as organic additive on the microstructure, texture and hardness was studied. The addition of the saccharin to the plating baths eliminated the texture and yielded very fine microstructures with high dislocation densities and twin fault probabilities for all solution types tested. A strong correlation was found between the defect density and the grain size.

A plating bath based on nickel sulfate and sodium citrate was developed for the deposition of crack-free Ni–Mo alloy layers of $d > 20$ mmthickness with varying Mo content up to 6 mol%. The increase in the Mo content resulted in a larger dislocation density and twin fault probability as well as a smaller grain size. The presence of saccharin as additive in the bath and the incorporated sulfur content due to the saccharin decomposition led to a further decrease in the grain size. The Mo content of the alloy improved the thermal stability of the alloys, while the sulfur incorporation had an adverse effect. The sulfur-free $Ni_{94}Mo_6$ alloy conserved its nanocrystalline nature with < 50 nm grain size up to 800 K, even though the twin faults and the dislocations annihilate under this annealing condition.

(All works related to the structural studies were performed in co-operation with the Eötvös University and the Centre for Energy Research of the Hungarian Academy of Sciences.)

Industry-oriented research activities. — Electrodeposition has long been playing a vital role in surface finishing by being able to produce a variety of metallic coatings on product surfaces for protective, decorative and various other functional purposes. At a certain level of technological development, there was an increasing demand for coatings with improved deposit performance. This need was the driving force behind the elaboration of new electrodeposition methods which enable the preparation of coatings with their composition varying along the thickness. Such “compositionally graded coatings” can be classified as compositionally modulated alloys (CMA) or multilayers. In the case of a CMA coating, the alloy deposit composition is continuously modulated along the thickness. In the case of a multilayer coating, the deposit consists of an alternating sequence of two layers with different chemical compositions whereby the constituent individual layers can have a thickness even down to the nanometer scale (for metallic materials, 1 nm corresponds to roughly 4-5 monatomic layers). In collaboration with the Hirtenberger Engineered Surfaces (HES), Austria, we have provided an overview of the development of various pulse-plating methods for the preparation of compositionally graded coatings from a single bath. As a particular case, the historical development of corrosion-protective electrodeposited multilayers based on the Zn-Fe system and their state of the art was exemplified. This overview was presented at the last European Pulse Plating Seminar in Vienna, organized by biannually by HES and was published as a review paper in one of the leading journal of industrial surface finishing.

Calculations taking into account various chemical equilibra (acid-base, complex formation and partition between phases) were performed in order to establish a technique combining dual-phase potentiometric lipophilicity measurement with the partition coefficient method. With a negligible simplification, a linear equation was obtained for calculating both the acid dissociation and the complex formation constants. The method developed proved to be suitable for testing the lipophilicity of drug candidates by using smaller quantities and much less expensive instrumentation than conventional techniques. The complex-formation constants obtained for all drug candidate compounds tested reproduced very well the values reported by using other methods. (This work was performed in co-operation with the following partners: Compound Profiling Laboratory of the Gedeon Richter Plc., Budapest University of Technology and Economics and Cyclolab Cyclodextrin Research and Development Ltd.)

2017

Granular materials – Flow, jamming and segregation phenomena in sheared systems. — Segregation is often observed in granular mixtures due to size or weight difference of the grains. It is well known that heavier or smaller grains migrate downwards in a granular shear flow. We have shown, that grains differing only in surface friction (size and weight is the same) also segregate when sheared, where smooth grains accumulate in the lower regions of the shear zone (Fig. 1). Moreover, when gravity is negligible to other (compressional) forces, the sample still segregates with the smooth grains leaving the shear zone.

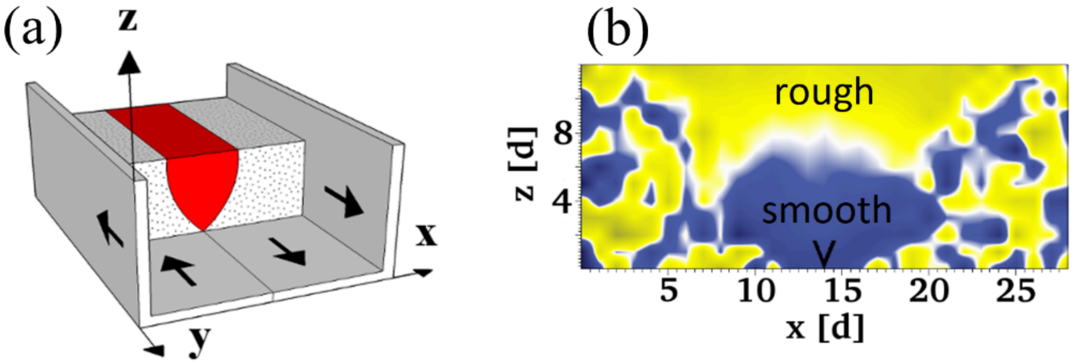

__Figure 1.__ A mixture of smooth and rough beads is sheared. Smooth beads migrate to the bottom of the shear zone due to kinetic sieving.

The flow of elongated grains has been also studied in experiments and numerical simulations. We have experimentally shown, that the flow rate of a hopper is slightly decreased and clogging probability is higher for rod like particles compared to spheres. In numerical simulations, the effective friction of an assembly of frictionless spherocylinders was a non-monotonic, but predominantly decreasing function of the particle aspect ratio.

Two distinct strain amplitudes have been identified in soft glassy materials, such as emulsions, foams, suspensions and pastes, close to the jamming transition. Numerical simulations of oscillatorily sheared soft sphere packings revealed that as the strain amplitude is increased, the initially elastic systems undergo a softening transition, at which both the elastic and loss moduli drop and reach a new plateau. Increasing the strain amplitude further causes yielding, marked by diffusive particle trajectories.

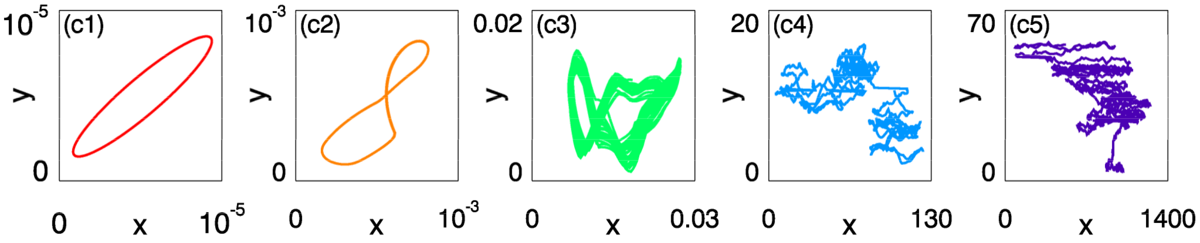

__Figure 2.__ Representative particle trajectories in oscillatory shear. For increasing shear amplitude (left to right), the elliptic trajectory corresponding to linear elasticity becomes non-periodic, but still bounded (softening), then diffusive (yielding).

Liquid crystals. — Tunable optical gratings based on the flexoelectric effect were created in a bent-core nematic liquid crystal. The wavelength of the structure was controlled by the applied d.c. voltage, as demonstrated by polarizing microscopy and light diffraction techniques (Fig. 3): higher voltage yields shorter wavelength. Visibility of the diffraction orders depended on the polarization of the illuminating laser beam (Fig. 4). The dynamical response of the system to switching between voltage levels were also explored. The characteristics and the mechanisms of switching were found to be different, depending on whether the lower voltage level is below or above the threshold of pattern onset. In both cases, the response to increasing voltage levels was much slower than that to decreasing ones.

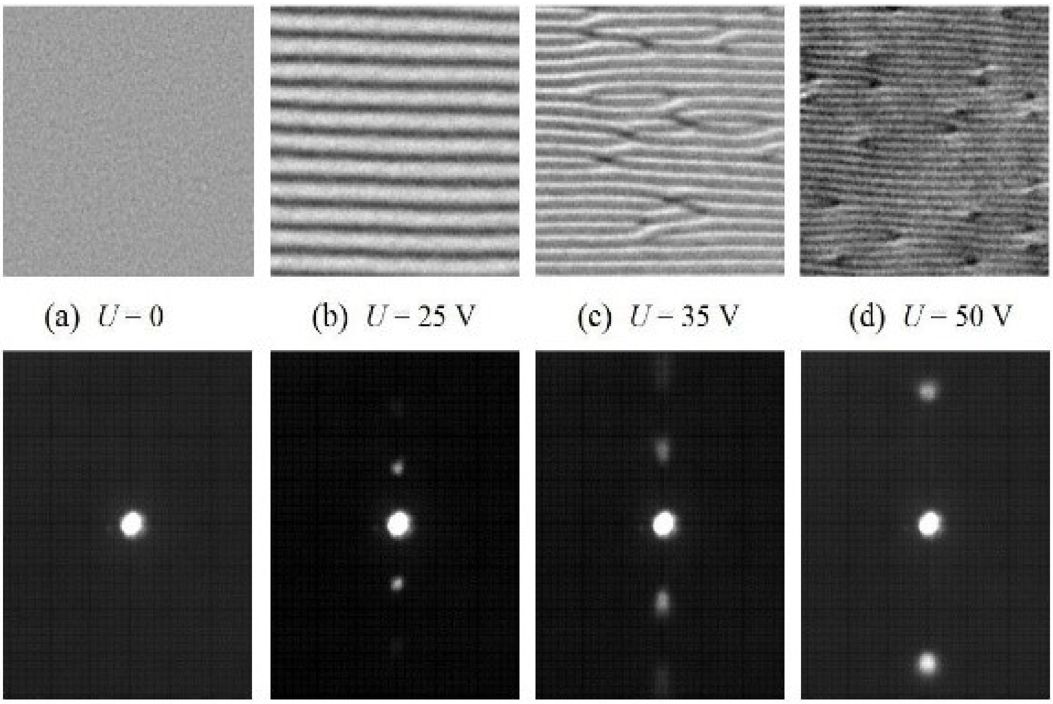

Figure 3. *Microphotographs and diffraction patterns of flexodomain gratings at increasing applied voltages.*

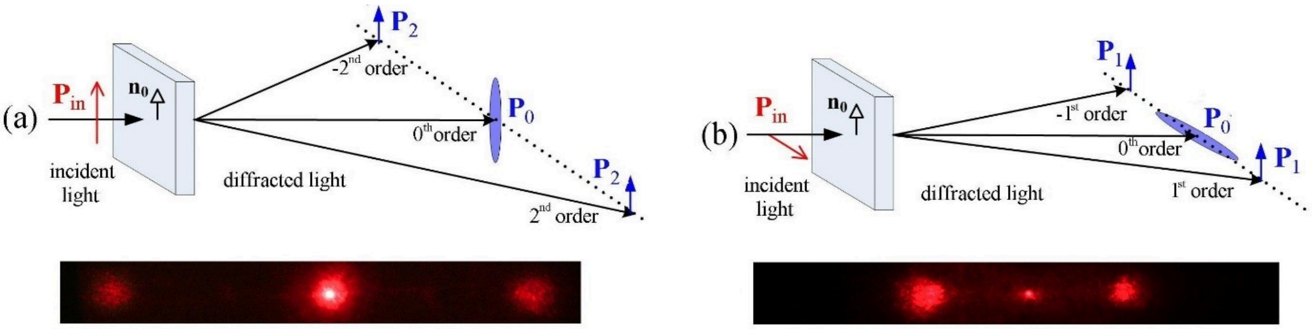

Figure 4. *Diffraction geometries and the corresponding diffraction images at (a) extraordinary and (b) ordinary illumination.*

Liquid crystal composite materials. — Structural transitions under the combined action of magnetic and electric fields have been monitored in 6CHBT and 6CB liquid crystal-based ferronematics, obtained by doping the nematics with spherical and rod-like magnetic nanoparticles in low (≤ 10-4) volume concentrations. Based on the experimental data, the type of the anchoring at the liquid crystal-nanoparticle interface (rigid or soft), as well as the mutual orientation of the magnetic moment of the nanoparticles and the nematic director have been determined.

Studies of the effect discovered the previous year, namely the increase of the alternating current magnetic susceptibility of ferronematics, induced by a dc bias magnetic field applied in the isotropic phase, which vanishes irreversibly when the ferronematic is cooled down to the nematic phase, have been continued. With the optimization of the ferronematic composition, the range of the d.c. bias magnetic field to which the ferronematic is sensitive without saturation was increased by about two orders of magnitude. This finding paves a way to application possibilities such as low magnetic field sensors or basic logical elements for information storage.

2017

Oscillating electrochemical reactions. — Samples containing alternating Co-rich and Mn-B-O layers were prepared by oscillating electrochemical reaction in collaboration with the Institute of Physical Chemistry of the Bulgarian Academy of Sciences. The preliminary cyclic voltammetric study of the solution containing CoSO4, MnSO4 and H3BO3 revealed that the manganese-containing layer is formed by a precipitation-like process due to the alkalination of the cathode vicinity during the hydrogen evolution.

A detailed analysis of the current oscillation was performed by using fast Fourier transformation. The oscillation was stable typically for more than 20 minutes. The current oscillation was anharmonic and exhibited a double maximum pattern. A few current oscillations are depicted in Fig. 1.a with the fast Fourier transform of the current–time function of a 80 s section in Fig. 1.b.

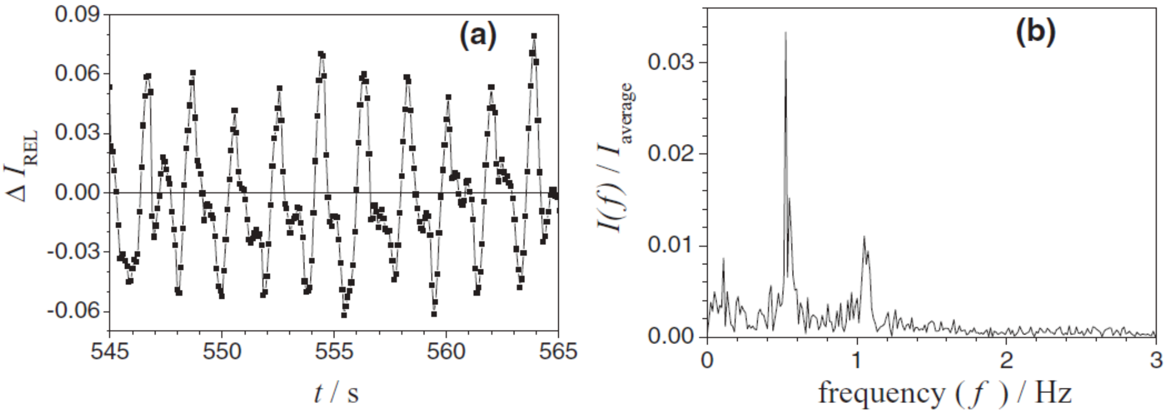

***Figure 1.** (a) Typical current oscillations obtained and (b) the fast Fourier transform of an 80-second-long section of the current–time function that comprises the data shown in Fig.1(a).*

The stability of the oscillation was characterized by the ratio of the two characteristic frequency maxima and the full width at the half maxima of the peak in the fast Fourier spectra. It can be seen in Fig. 2 that the current oscillation does not only prevail for a long time but it is also stabilized, as the decrease in the width of the frequency peaks in time indicates.

The magnetic analysis of the deposits revealed a superparamagnetic behavior of the samples. The size of the magnetic entities as calculated from the Langevin fit of the magnetization curves was in accord with the magnetic layer thickness calculated from the current density and the length of the oscillation period.

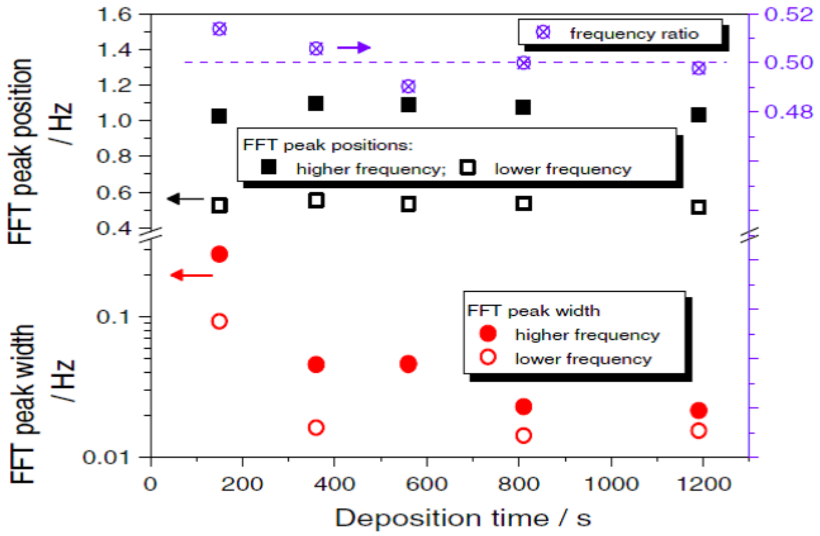

Figure 2. *Key parameters of the stability of the electrochemical oscillation.*

Magnetism and electronic structure of Ni-metalloid amorphous alloys. — The paramagnetic (PM) to ferromagnetic (FM) transition has been previously investigated on numerous (Ni100-xFex)-MD alloys upon the introduction of Fe where MD can represent a combination of various metalloid elements (P, B, Al, Si), while keeping the metal/metalloid ratio constant. Adding a sufficient amount of Fe to a Pauli PM Ni-MD alloy matrix first induces a spin-glass (SG) state at low temperatures which goes over to a PM state at higher temperatures. Beyond a critical Fe content, xc, the SG state transforms to a FM state upon increasing the temperature. By plotting the characteristic transition temperatures as a function of the Fe content, a magnetic phase diagram (Fig. 3) can be constructed for each Ni-Fe-MD system which has a multicritical point (MCP) at xc. It has been now shown that by using the reported magnetic phase diagrams of various Ni-Fe-MD alloy systems, the critical Fe content, xc, for the onset of ferromagnetic order scales inversely with the density of states at the Fermi level, N(EF), of the parent Ni-MD matrix. This means that the higher the N(EF), the lower the critical Fe content to induce ferromagnetism in the Ni-MD matrix. This is because a higher N(EF) leads to a higher Stoner enhancement factor, S, which characterizes the tendency of the matrix to become ferromagnetic. If S is higher for a Ni-MD matrix, a smaller amount of Fe atoms is able to develop an exchange interaction with each other and with the Ni atoms to drive the system to an FM state. Along this line, the critical Fe concentration was found to scale also with S, and the same was found to hold also for the multicritical temperature, TMCP.

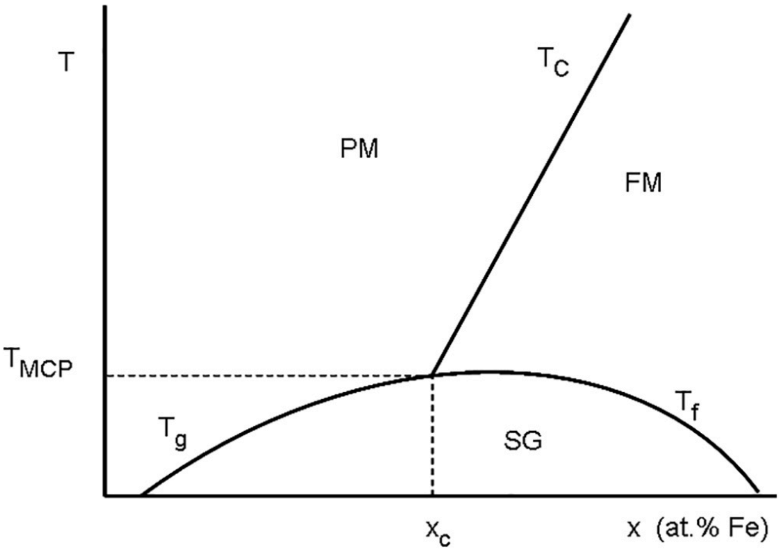

Figure 3. *Schematic view of the magnetic phase diagram for (Ni100-xFex)-MD amorphous alloys.*

Corrosion studies. — Long-term corrosion tests were performed for welded 18Ni-10Cr austenitic stainless steel pipes. The model experiment simulated the impact of the differential ventilation conditions with a large cathode/anode surface area ratio and the enhanced corrosion sensitivity of the welded area. The schematic picture of the experimental setup is shown in Fig. 4. The 46-day-long experiment revealed that under the differential ventilation conditions, pitting corrosion can occur also at the time scale of months on a material that is designed to be in service for decades. It was also found that the solute in the corrosion medium (a boric acid solution that is analogous to some bath used in the nuclear industry) cannot prevent the occurrence of microbiologically induced corrosion processes since the reproduction of bacteria and their biofilm-forming activity is not blocked.

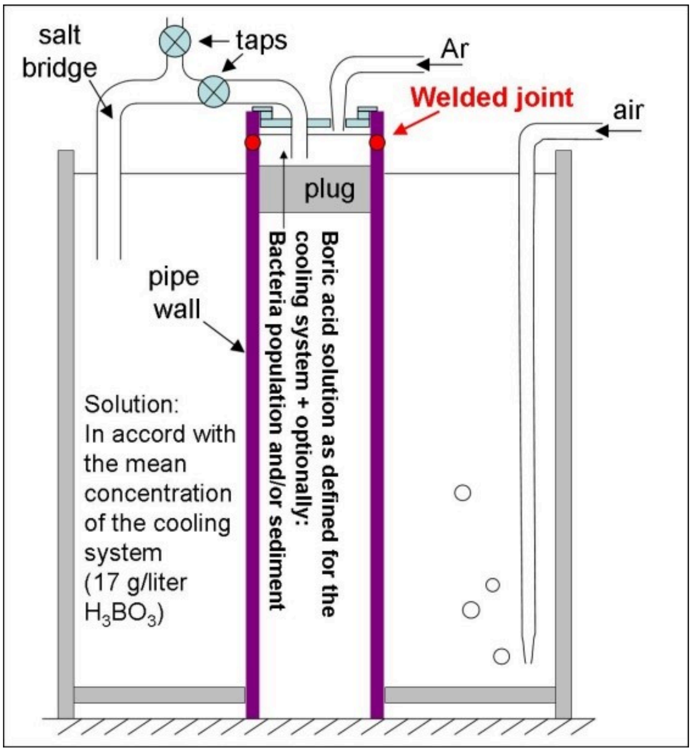

Figure 4. *Setup of the corrosion test device with the application of differential ventilation conditions and a high cathode/anode surface area ratio. The height of the device was 1 meter.*